1   **Deep Atlantic Ocean carbon storage and the rise of 100,000-year glacial cycles**

2

3   J.R. Farmer[1,2,3,4]*, B. Hönisch[1,2], L.L. Haynes[1,2], D. Kroon[5], S. Jung[5], H.L. Ford[2,6], M.E.

4   Raymo[1,2], M. Jaume-Seguí[2,7], D.B. Bell[5], S.L. Goldstein[1,2], L.D. Pena[7], M. Yehudai[1,2],

5   and J. Kim[2]

6   [1]Department of Earth and Environmental Sciences, Columbia University, USA

7   [2]Lamont-Doherty Earth Observatory of Columbia University, USA

8   [3]now at Department of Geosciences, Princeton University, USA

9   [4]now at Max-Planck Institut für Chemie, Mainz, Germany

10   [5]School of GeoSciences, University of Edinburgh, UK

11   [6]School of Geography, Queen Mary University of London, UK

12   [7]Department of Earth and Ocean Dynamics, University of Barcelona, Spain

13   *Corresponding Author: jesse.farmer@princeton.edu

14
15   Text: 2,592 words
16   Methods: 2,942 words
17   Figures: Four (three two-column 180 mm, one one-column 88 mm)
18   Figure Legends: 563 words

19 **Over the past three million years, Earth's climate oscillated between warmer**

20 **interglacials with reduced terrestrial ice volume and cooler glacials with expanded**

21 **polar ice sheets. These climate cycles, as reflected in benthic foraminiferal oxygen**

22 **isotopes, transitioned from dominantly 41-kyr to 100-kyr periodicities during the**

23 **mid-Pleistocene (1,250 to 700 ka). Because orbital forcing did not shift at this time,**

24 **the ultimate cause of this mid-Pleistocene transition (MPT) remains enigmatic. Here**

25 **we present foraminiferal trace element (B/Ca, Cd/Ca) and Nd isotope data that**

26 **demonstrate a tight linkage between Atlantic Ocean meridional overturning**

27 **circulation and deep-ocean carbon storage across the MPT. Specifically, between**

28 **950 and 900 ka, carbonate ion saturation decreased by 30 μmol/kg and phosphate**

29 **concentration increased by 0.5 μmol/kg coincident with a 20% reduction of North**

30 **Atlantic Deep Water contribution to the abyssal South Atlantic. These results**

31 **demonstrate that the glacial deep Atlantic carbon inventory increased by**

32 **approximately 50 gigatons during the transition to 100-kyr glacial cycles. We**

33 **suggest that the coincidence of our observations with evidence for increased**

34 **terrestrial ice volume reflects how weaker overturning circulation and Southern**

35 **Ocean biogeochemical feedbacks facilitated deep ocean carbon storage, which**

36 **lowered atmospheric pCO_2 and thereby enabled expanded terrestrial ice volume at**

37 **the MPT.**

38   Cyclic glaciations are the primary feature of Earth's climate since the late

39 Pliocene and occur at periodicities linked to variations in solar insolation[1]. However, the

40 dominant periodicity of glaciations transitioned from 41-kyr to 100-kyr during the mid-

41 Pleistocene without concomitant changes in external insolation forcing[2-5]. It has been

42 suggested that the emergence of high-amplitude 100-kyr cycles in surface and deep ocean

43 climate records during the MPT[4,5,6] relates to internal climate amplifiers ("feedbacks")[3],

44 including changes in ice sheet dynamics[3,5,6-11], ocean circulation[12,13], and interactions of

45 these processes with Earth's carbon cycle[10-14]. Although temporal resolution is low,

46 atmospheric pCO_2 reconstructions across the MPT show that glacial pCO_2 decreased by

47 ~30 µatm sometime between 1,000 and 800 ka[11,15,16], consistent with more voluminous

48 glacial ice sheets[10,17]. The missing glacial pCO_2 was most likely sequestered in the deep

49 ocean[18] as suggested by benthic foraminiferal carbon isotope records ($\delta^{13}C_b$)[5,14,19].

50 However, evidence from $\delta^{13}C_b$ reflects a combination of ocean circulation, air-sea gas

51 exchange, and ocean carbon content, which complicates quantitative reconstructions of

52 any one parameter[13,14,19]. Because reliable quantitative records of ocean carbonate

53 chemistry are sparse, it is debated how the ocean sequestered additional CO_2 at the

54 MPT[11,13]. Stronger quantitative constraints on deep ocean dissolved inorganic carbon

55 (DIC) and its relation to meridional overturning circulation (MOC) are needed to evaluate

56 whether, and by which mechanisms, the ocean stored additional carbon at the MPT.

57   Here we test the hypothesis that the onset of 100-kyr glacial cycles during the

58 MPT was facilitated by enhanced deep ocean carbon storage accommodated by reduced

59 Atlantic MOC[12,13]. We present the first paired reconstructions of deep ocean DIC content

60 and MOC using foraminiferal trace element (B/Ca, Cd/Ca) and Nd isotope proxies,

61 recorded in sediments from Ocean Drilling Program Site 1267 from the Southeast

62 Atlantic Ocean (Fig. 1). In combination with previously published MOC and trace

63 element reconstructions, our results indicate coeval MOC reduction and increased deep

64 Atlantic DIC after 950 ka. We evaluate the contribution of our DIC estimates to

65   atmospheric pCO$_2$ based on ocean CO$_2$ sequestration mechanisms identified by modeling

66   studies of the Last Glacial Maximum (LGM, ~20 ka), and hypothesise a sequence of

67   climatic events that link changes in ocean circulation, carbon cycle and Earth's

68   cryosphere with the emergence of 100-kyr glacial cycles during the MPT.

69   **Carbonate chemistry, nutrients, and MOC across the MPT**

70   Site 1267 is located at 4.4 km water depth in the Angola Basin north of Walvis

71   Ridge[20], within dense Atlantic Ocean bottom waters (Fig. 1b). These waters comprise

72   two general endmembers with characteristic chemical properties: North Atlantic Deep

73   Water (NADW) feeds the basin from the north, and Antarctic Bottom Water (AABW)

74   from the south. High oxygen, low-CO$_2$ and nutrient-poor NADW carries a low Nd

75   isotope ratio (expressed as more negative ε_{Nd}, Methods), while low oxygen, high-CO$_2$

76   and nutrient-replete AABW carries a more positive ε_{Nd} signature from admixed Pacific

77   waters (Fig. 1). Because Walvis Ridge blocks AABW inflow from the south, AABW

78   enters the Angola Basin via the Romanche Fracture zone (0°N), thereby limiting the

79   contribution of the generally deeper AABW to abyssal Angola Basin waters today (Fig.

80   1b). However, Site 1267 exhibits higher nutrient conditions (indicated by low $\delta^{13}C_b$

81   values) during Pleistocene glaciations[21,22], suggesting that this location tracks the balance

82   of NADW and AABW contributions to the deep Atlantic across the MPT.

83   The B/Ca and Cd/Ca ratios of the epibenthic foraminifer *Cibicidoides*

84   *wuellerstorfi* reflect the deep-sea carbonate ion saturation state[23] ($\Delta[CO_3^{2-}]$) and

85   phosphate concentration[24] ($[PO_4^{3-}]$), respectively (Methods). Changes in $\Delta[CO_3^{2-}]$ and

86    $[PO_4^{3-}]$ are linked to changes in DIC through ocean biogeochemistry, and we apply these

87 proxies from Site 1267 alongside published B/Ca and Cd/Ca records from North Atlantic

88 Site 607[13,25] to quantitatively constrain deep Atlantic DIC across the MPT. Additionally,

89 ε_{Nd} of planktic foraminiferal Fe-Mn oxide coatings at Site 1267 records the local

90 expression of changes in NADW and AABW contributions to the deep Atlantic Ocean

91 and complements a more southerly reconstruction of MOC strength across the MPT[12].

92   Site 1267 geochemical data show pronounced shifts in circulation and chemical

93 properties between Marine Isotopic Stages (MIS) 26 (970 ka) and 22 (880 ka) (Fig. 2).

94 ε_{Nd} suggests an ~20% reduction in NADW contribution to the South Atlantic between

95 MIS 26/25 and MIS 23/22 (Methods), in agreement with records from Sites 1088 and

96 1090 located ~10° to the south[12] (Supplementary Fig. 1). These combined ε_{Nd} records

97 indicate that the MOC perturbation between MIS 26 and 22 exceeds any previously

98 studied glacial transition before 950 ka. This MOC reduction corresponds with abrupt

99 increases in deep water corrosivity and nutrient content as indicated by an ~30 µmol/kg

100 $\Delta[CO_3^{2-}]$ decrease and an ~0.5 µmol/kg $[PO_4^{3-}]$ increase at Site 1267 (Fig. 2c, d). This

101 chemical transition persisted for at least 500 kyr. Whereas bottom water $\Delta[CO_3^{2-}]$ was

102 near or above saturation ($\Delta[CO_3^{2-}] = 0$) prior to 950 ka, $\Delta[CO_3^{2-}]$ values after 950 ka were

103 consistently negative in both glacials and interglacials, and they equaled modern $\Delta[CO_3^{2-}]$

104 of -2 µmol/kg during interglacials MIS 19, 17, and 13 (Fig. 2c). Similarly, reconstructed

105 $[PO_4^{3-}]$ was significantly higher after 950 ka than before, and approached modern $[PO_4^{3-}]$

106 of 1.6 µmol/kg during MIS 19, 17, and 13 (Fig. 2d).

107   The B/Ca and Cd/Ca patterns displayed by our Site 1267 records are similar in

108 trend but more pronounced than observations at Site 607 in the North Atlantic[13,25] (Fig.

109 2c, d). Site 607 $\Delta[CO_3^{2-}]$ is higher and $[PO_4^{3-}]$ lower than at Site 1267 for the length of

110   the records (Fig. 2), consistent with continuously better ventilation in the deep North

111   Atlantic compared to the abyssal Southeast Atlantic between 1,400 and 400 ka.

Quantifying deep Atlantic DIC increase

113   Synchronous but opposing $\Delta[CO_3^{2-}]$ and $[PO_4^{3-}]$ reconstructions across the MPT

114   (Fig. 2c-d) suggest the deep Atlantic acquired additional respired carbon after 950 ka.

115   Whereas $[PO_4^{3-}]$ proportionally increases with DIC through the stoichiometric ratio of

116   carbon to phosphorous in organic matter[26], the CO_2 released during respiration decreases

117    $[CO_3^{2-}]$, lowering $\Delta[CO_3^{2-}]$ (Supplementary Fig. 2). Using the C:P ratio of organic matter

118   exported to the deep ocean (117±14:1, ref. 26), and making simplifying assumptions

119   about changes in Cd inventory and seawater Cd:P ratios (Supplementary Information),

120   we quantify deep Atlantic DIC change associated with the MOC shift around 950 ka

121   (MIS 25) in glacial and interglacial climates (Methods). In addition, we also estimate

122   DIC change from $\Delta[CO_3^{2-}]$ by assuming constant local alkalinity (following ref. 27,

123   Methods).

124   At South Atlantic Site 1267, glacial DIC after 950 ka increased by 50±16

125   µmol/kg reconstructed from $\Delta[CO_3^{2-}]$, and 49±24 µmol/kg from $\Delta[PO_4^{3-}]$, compared to

126   glacials before 950 ka (Fig. 3a, b). At North Atlantic Site 607, glacial DIC similarly

127   increased by 50±30 µmol/kg reconstructed from $\Delta[CO_3^{2-}]$, and 20±18 µmol/kg from

128    $\Delta[PO_4^{3-}]$ (all uncertainties 1s). Reconstructed DIC also increased during interglacials

129   after 950 ka; at Site 1267 by 44±24 µmol/kg from $\Delta[CO_3^{2-}]$ and by 42±16 µmol/kg from

130    $\Delta[PO_4^{3-}]$; at Site 607 by 23±23 µmol/kg from $\Delta[CO_3^{2-}]$ and by 10±18 µmol/kg from

131    $\Delta[PO_4^{3-}]$ (Fig. 3). The averaged deep Atlantic glacial DIC increase after 950 ka (42±15

132   μmol/kg) agrees with the 42±22 μmol/kg DIC increase reconstructed from benthic

133   foraminiferal B/Ca between MIS 5a and 4 prior to the LGM[27]. The generally larger DIC

134   increases at Site 1267 (Fig. 3a, b) likely reflect the southerly and deeper position of Site

135   1267 relative to Site 607, which makes Site 1267 a more sensitive indicator of the relative

136   contributions of northern and southern sourced deep waters. Nevertheless, these similar

137   DIC estimates from two independent proxies at separate locations lend confidence for a

138   persistent deep Atlantic DIC increase after 950 ka that encompassed both glacial and

139   interglacial climates.

140   Increased DIC after 950 ka is likely the consequence of a more aged deep-water

141   body in the deep Atlantic, with accumulated respired CO_2 and nutrients. Nd isotope ratios

142   show that this aged deep water is associated with reduced NADW. Glacial ε_{Nd} values

143   became more positive after 950 ka at Sites 1088, 1090 and 1267 (Fig. 3c, Supplementary

144   Fig. 1), indicating reduced NADW and/or enhanced AABW. Interglacial ε_{Nd} values also

145   show more positive values after 950 ka compared with before MIS 23 at Site 1267,

146   indicating that reduced MOC after 950 ka was not limited to glacial climates (Methods).

147   Covariance between ε_{Nd}, $\Delta[CO_3^{2-}]$ and $[PO_4^{3-}]$ at Site 1267 confirms that MOC and

148   bottom water chemistry shifts are linked (Supplementary Fig. 3).

149   **Implications for atmospheric pCO$_2$**

150   As the Southern Ocean is the principal gateway for CO_2 to escape from the deep

151   Atlantic into the atmosphere, changes in surface Southern Ocean properties that affect

152   CO_2 leakage likely contribute to atmospheric CO_2 variations over Pleistocene glacial

153   cycles[28,29]. These processes have also been invoked for the MPT[30], with recent studies

154   proposing that expanded Southern Ocean sea-ice extent[13] or increased iron availability[11]

155   lowered pCO_2 across the MPT. Upon comparing the temporal relationships of the

156   evidence, we propose that MPT pCO_2 reduction was closely related with reduced MOC

157   (Fig. 3). Whereas glacial Subantarctic iron deposition gradually increased between 1,400

158   and 1,100 ka[31] (Fig. 3f), ice core and proxy reconstructions suggest glacial pCO_2 did not

159   decrease before 1,000 ka[11,15,16] (Fig. 3d). Instead, glacial pCO_2 most likely decreased at

160   MIS 24-22, coeval with increased deep Atlantic DIC (Fig. 3a-b), lowered sea-level at

161   MIS 22[10,17] (Fig. 3g), and global surface ocean cooling[5,6]. This implies that reduced pCO_2

162   conforms to the more extensive glacial ice sheets of the 100-kyr world. Our prediction

163   that glacial pCO_2 was primarily reduced during MIS 24 and 22 agrees with pCO_2

164   simulations[32,33], and is testable with more detailed pCO_2 reconstructions from this critical

165   interval.

166   Lower pCO_2 is plausibly linked to increased deep Atlantic DIC by more complete

167   Southern Ocean nutrient utilisation and/or increased deep ocean stratification[29,34,35] after

168   950 ka. As indicated above, we do not believe that iron fertilisation primarily drove lower

169   pCO_2 after 950 ka. Instead, the coherent timing with MOC suggests a circulation-driven

170   process. The Southern Ocean's residual overturning circulation is driven by surface

171   density fluxes[36], and it has been proposed that changes to these density fluxes in glacial

172   climates are dynamically linked to deep ocean stratification[35,37] and pCO_2[38]. Specifically,

173   reduced rates of surface water densification combined with a northward shift of Southern

174   Ocean upwelling during glacial climates[38] increases the surface ocean residence time of

175   nutrient-rich waters, enhancing nutrient utilisation and CO_2 uptake before new AABW is

176   formed[38]. Both stratification and enhanced nutrient utilisation would increase deep ocean

177   DIC by preferentially segregating regenerated products (nutrients and carbon) in the deep

178   ocean. Deep ocean $\Delta[CO_3^{2-}]$ consequently decreases, driving a transient carbonate

179   (CaCO$_3$) dissolution event[39] that may increase alkalinity and foster additional ocean CO_2

180   storage[40,41], although the mechanisms and timescales of such alkalinity feedbacks are

181   debated[25]. Accounting for an alkalinity increase slightly elevates our estimate of deep

182   Atlantic DIC increase from B/Ca, but does not fundamentally change our results

183   (Methods).

184   The above conceptual arguments are supported by similar magnitudes of pCO_2

185   reduction at the MPT and in LGM model simulations of reduced MOC coupled to

186   reduced Southern Ocean CO_2 outgassing. Assuming our pooled estimate of glacial DIC

187   increase (42±15 µmol/kg) characterised the entire deep Atlantic below 3 km, then its

188   carbon inventory increased by 51±18 Gt C during glaciations after 950 ka (Methods).

189   Quantifying pCO_2 reduction from this DIC increase requires simulating the new

190   equilibrium reached between the ocean and atmospheric C reservoirs following the DIC

191   increase. Model simulations of the LGM provide a comparable constraint where the

192   effects of MOC and reduced Southern Ocean CO_2 outgassing on deep Atlantic DIC and

193   pCO_2 are quantified. In these simulations, combining reduced MOC with reduced

194   Southern Ocean CO_2 outgassing increases deep ocean DIC through a stronger biological

195   pump[27,29,43] and lowers pCO_2 by 13 to 45 ppm[29,42,43]. The consistency between these

196   pCO_2 estimates and the reconstructed 20-40 ppm glacial pCO_2 decrease across the

197   MPT[11,15,16] (Fig. 3e) supports a MOC and Southern Ocean pathway for MPT glacial

198   pCO_2 reduction. This implies that the 'ventilation volume' CO_2 sequestration hypothesis

199   for the LGM[29,43] first initiated with the major glacial MOC reduction after 950 ka[12], and

200   drove lower glacial pCO_2 levels during ensuing 100-kyr glacial cycles (Fig. 4).

201   Our averaged estimate for interglacial DIC increase (30±16 µmol/kg) implies a

202   deep Atlantic carbon inventory increase of 36±20 Gt C during interglacials after 950 ka.

203   This evidence for greater interglacial deep ocean carbon storage after 950 ka may have

204   contributed to the ~30 to 40 ppm lower pCO_2 during the "lukewarm" interglacials

205   between 450 and 900 ka[15,44], although identifying mechanisms for this requires further

206   study.

207   **Perspective**

208   An enduring mystery surrounding the MPT is how the cryosphere, ocean, and

209   carbon cycle interacted to initiate 100-kyr climate cycles at this particular time in Earth

210   history. While erosion of Northern Hemisphere regolith has been a central hypothesis for

211   the MPT[5,7,9,11], we suggest that an expanded Antarctic Ice Sheet played a key role in

212   unleashing the ocean carbon cycle feedbacks necessary for 100-kyr cycles (Fig. 4).

213   Atmospheric cooling associated with growth of the East Antarctic Ice Sheet to marine-

214   based margins around 1000 ka[8,45] (Fig. 3e) would have enhanced the production and

215   export of Antarctic sea-ice[37], expanding the spatial extent[35,37] but reducing the intensity

216   of surface water densification around Antarctica[38]. This increased residence time of

217   nutrient-rich waters would have enhanced nutrient utilisation and therefore CO_2 uptake.

218   Increased Antarctic surface "buoyancy loss" may also have directly facilitated expanded

219   AABW and enhanced deep ocean stratification[35,37], although we cannot rule out Northern

220   Hemisphere forcing of the MOC shift through reduced NADW production (Fig. 4c).

221   Future studies of Southern Ocean nutrient utilisation and deep ocean stratification across

222   the MPT can elucidate how these two mechanisms contributed to MPT pCO_2 decline.

223   In summary, our results demonstrate that the rise of 100-kyr ice age cycles is

224   intimately linked with increased deep ocean carbon storage associated with weakened

225   MOC. The key roles for ocean circulation and the carbon cycle in the natural climate

226   transition at the MPT raise critical questions on the future behaviour of these climate

227   components under anthropogenic warming. By the end of the century, Atlantic MOC is

228   projected to decrease by potentially similar magnitude (~20%) as the MOC reduction at

229   the MPT, albeit with high uncertainty[46,47]. While we have demonstrated that a weaker

230   MOC related to increased deep ocean carbon storage at the MPT, future deep ocean

231   carbon sequestration depends on how future MOC interacts with the evolution of the

232   biological pump and deep ocean stratification. In contrast to the MPT, projected future

233   reductions of Southern Ocean surface density[37,48] and reduced anthropogenic CO_2 uptake

234   by NADW under MOC weakening[49] may diminish the future carbon sequestration

235   potential of the deep Atlantic Ocean.

236

237   **References**

238   1. Hays, J.D., Imbrie J. & Shackleton, N. Variations in the Earth's Orbit: Pacemaker of

239   the Ice Ages. *Science* **194**, 1121-1132 (1976)

240   2. Pisias, N. & Moore, T. The evolution of Pleistocene climate: A time series approach.

241   *Earth Planet. Sci. Lett.* **52**, 450-458 (1981)

242   3. Imbrie, J. *et al*. On the structure and origin of major glaciation cycles 2. The 100,000-

243   year cycle. *Paleoceanography* **8**, 699-735 (1993).

244   4. Ruddiman, W.F., Raymo, M.E., Martinson, D.G., Clement, B.M. & Backman, J.

245   Pleistocene Evolution: Northern Hemisphere ice sheets and North Atlantic Ocean.

246   *Paleoceanography* **4**, 353-412 (1989).

247   5. Clark, P.U. *et al.* The middle Pleistocene transition: Characteristics, mechanisms, and

248   implications for long-term changes in atmospheric pCO_2. *Quat. Sci. Rev.* **25**,

249   3150-3184 (2006).

250   6. McClymont, E.L., Sosdian, S.M., Rossell-Melé, A. & Rosenthal, Y. Pleistocene sea-

251   surface temperature evolution: Early cooling, delayed glacial intensification, and

252   implications for the mid-Pleistocene climate transition. *Earth-Sci. Rev.* **123**, 173-

253   193 (2013).

254   7. Clark, P.U. & Pollard, D. Origin of the Middle Pleistocene Transition by ice sheet

255   erosion of regolith. *Paleoceanography* **13**, 1-9 (1998).

256   8. Raymo, M.E., Lisiecki, L.E. & Nisancioglu, K.H. Plio-Pleistocene Ice Volume,

257   Antarctic Climate, and the Global $\delta^{18}O$ Record. *Science* **313**, 492-495,

258   doi:10.1126/science.1123296 (2006).

259   9. Sosdian, S. & Rosenthal Y. Deep-Sea Temperature and Ice Volume Changes Across

260   the Pliocene-Pleistocene Climate Transitions. *Science* **325**, 306-310,

261   doi:10.1126/science1169938 (2009).

262   10. Elderfield, H. *et al.* Evolution of Ocean Temperature and Ice Volume Through the

263   Mid-Pleistocene Climate Transition. *Science* **337**, 704-709 (2012).

264   11. Chalk, T.B., Hain, M.P. *et al.* Causes of ice age intensification across the Mid-

265   Pleistocene Transition. *Proc. Natl. Acad. Sci.* **114**, 13114-13119,

266   doi:10.1073/pnas.1702143114 (2017).

267   12. Pena, L.D. & Goldstein, S.L. Thermohaline circulation crisis and impacts during the

268   mid-Pleistocene transition. *Science* **345**, 318-322, doi:10.1126/science.1249770

269   (2014).

270   13. Lear, C.H. *et al.* Breathing more deeply: Deep ocean carbon storage during the mid-

271   Pleistocene climate transition. *Geology* **44**, 1035-1038, doi:10.1130/G38636.1

272   (2016).

273   14. Hodell, D.A., Venz, K.A., Charles, C.D. & Ninnemann, U.S. Pleistocene vertical

274   carbon isotope and carbonate gradients in the South Atlantic sector of the

275   Southern Ocean. *Geochem. Geophys. Geosyst.* **4**, 1004 (2003).

276   15. Hönisch, B., Hemming, N.G., Archer, A., Siddall, M. & McManus, J.F. Atmospheric

277   carbon dioxide concentration across the mid-Pleistocene transition. *Science* **324**,

278   1551-1554 (2009).

279   16. Higgins, J.A. *et al.* Atmospheric composition 1 million years ago from blue ice in the

280   Allan Hills, Antarctica. *Proc. Natl. Acad. Sci.* **112**, 6887-6891,

281   doi:10.1073/pnas.1420232112 (2015).

282 17. Rohling, E.J., Foster, G.L., Grant, K.M., Marino, G., Roberts, A.P., Tamisiea, M.E. &

283   Williams, F. Sea-level and deep-sea-temperature variability over the past 5.3

284   million years. *Nature* **508**, 477-482 (2014).

285 18. Broecker, W.S. Glacial to interglacial changes in ocean chemistry. *Prog. Oceanog.* **11**,

286   151-197 (1982).

287 19. Raymo, M.E., Oppo, D.W. & Curry, W. The mid-Pleistocene climate transition: A

288   deep sea carbon isotopic perspective. *Paleoceanography* **12**, 546-559 (1997).

289 20. Zachos, J. *et al*. Site 1267. *Proc. ODP, Init. Repts.* **208**, 1-77 (2004).

290 21. Bell, D.B., Jung, S.J.A., Kroon, D., Lourens, L.J., & Hodell, D.A. Local and regional

291   trends in Plio-Pleistocene δ^{18}O records from benthic foraminifera. *Geochem.*

292   *Geophys. Geosyst.* **15**, 3304-3321 (2014).

293 22. Bell, D.B., Jung, S.J.A. & Kroon, D. The Plio-Pleistocene development of Atlantic

294   deep-water circulation and its influence on climate trends. *Quat. Sci. Rev.* **123**,

295   265-282, doi: 10.1016/j.quascirev.2015.06.026 (2015).

296 23. Yu, J. & Elderfield, H. Benthic foraminiferal B/Ca ratios reflect deep water carbonate

297   saturation state. *Earth Planet. Sci. Lett.* **258**, 73-86 (2007).

298 24. Boyle, E.A. Cadmium and δ^{13}C paleochemical distributions during the stage 2

299   Glacial Maximum. *Annu. Rev. Earth Planet. Sci.* **20**, 245-287 (1992).

300   25. Sosdian, S.M., Rosenthal, Y. & Toggweiler, J.R. Deep Atlantic Carbonate Ion and

301            $CaCO_3$ Compensation During the Ice Ages. *Paeloceanography and*

302   *Paleoclimatology* **33**, 546-562, doi:10.1029/2017PA003312 (2018).

303   26. Anderson, L.A. & Sarmiento, J.L. Redfield ratios of remineralization determined by

304   nutrient data analysis. *Global Biogeochem. Cycles* **8**, 65-80 (1994).

305   27. Yu, J. *et al.* Sequestration of carbon in the deep Atlantic during the last glaciation.

306   *Nature Geoscience* **9**, 319-324 (2016).

307   28. Sigman, D.M., Hain, M.P. & Haug, G.H. The polar ocean and glacial cycles in

308   atmospheric CO_2 concentration. *Nature* **466**, 47-55, doi:10.1038/nature09149

309   (2010).

310   29. Hain, M.P., Sigman, D.M., & Haug, G.H. Carbon dioxide effects of Antarctic

311   stratification, North Atlantic Intermediate Water formation, and Subantarctic

312   nutrient drawdown during the last ice age: Diagnosis and synthesis in a

313   geochemical box model. *Global Biogeochem. Cycles* **24**, GB4023 (2010).

314   30. Kemp, A.E.S, Grigorov, I., Pearce, R.B. & Naveira Garabato, A.C. Migration of the

315   Antarctic Polar Front through the mid-Pleistocene transition: evidence and

316   climatic implications. *Quat. Sci. Rev.* **29**, 1993-2009 (2010).

317   31. Martínez-Garcia, A. *et al*. Southern Ocean dust-climate coupling over the past four

318   million years. *Nature* **476**, 312-315, doi:10.1038/nature10310 (2011).

319   32. Köhler, P. & Bintanja, R. The carbon cycle during the Mid Pleistocene Transition:

320   The Southern Ocean Decoupling Hypothesis. *Clim. Past* **4**, 311-332, clim-

321   past.net/4/311/2008 (2008).

322   33. Lisiecki, L.E. A benthic δ^{13}C-based proxy for atmospheric pCO_2 over the last 1.5 Myr.

323   *Geophys. Res. Lett.* **37**, L21708, doi:10.1029/2010GL045109 (2010).

324   34. Adkins, J.F. The role of deep ocean circulation in setting glacial climates.

325   *Paleoceanography* **28**, 1-23, doi:10.1002/palo.20046 (2013).

326   35. Ferrari, R. *et al.* Antarctic sea ice control on ocean circulation in present and glacial

327   climates. *Proc. Natl. Acad. Sci.* **111**, 8753-8758, doi:10.1073/pnas.1323922111

328   (2014).

329   36. Marshall, J. & Speer, K. Closure of the meridional overturning circulation through

330   Southern Ocean upwelling. *Nature Geoscience* **5**, 171-180, doi:10.1038/ngeo1391

331   (2012).

332   37. Jansen, M.F. Glacial ocean circulation and stratification explained by reduced

333   atmospheric temperature. *Proc. Natl. Acad. Sci.* **114**, 45-50 (2017).

334   38. Watson, A.J., Vallis, G.K., & Nikurashin, M. Southern Ocean buoyancy forcing of

335   ocean ventilation and glacial atmospheric CO_2. *Nature Geoscience* **8**, 861-864

336   (2015).

337   39. Broecker, W.S. & Peng, T.-H. The role of $CaCO_3$ compensation in the glacial to

338   interglacial atmospheric CO_2 change. *Global Biogeochem. Cycles* **1**, 15-29 (1987).

339   40. Boyle, E.A. Vertical oceanic nutrient fractionation and glacial/interglacial CO_2 cycles.

340   *Nature* **331**, 55-56 (1988).

341   41. Archer, D. & Maier-Reimer, E. Effect of deep-sea sedimentary calcite preservation

342   on atmospheric CO_2 concentration. *Nature* **367**, 260-263 (1994).

343   42. Brovkin, V., Ganopolski, A., Archer, D. & Rahmstorf, S. Lowering of glacial

344   atmospheric CO_2 in response to changes in oceanic circulation and marine

345   biogeochemistry. *Paleoceanography* **22**, PA4204, doi:10.1029/2006PA001380

346   (2007).

347   43. Hain, M.P., Sigman, D.M. & Haug, The Biological Pump in the Past in *Treatise on*

348   *Geochemistry* 2nd edn, Vol. 8(18) (eds Mottl, M. J. & Elderfield, H.) 485–517

349   (2013).

350   44. Lüthi, D. *et al.* High-resolution carbon dioxide concentration record 650,000-800,000

351   years before present. *Nature* **453**, 379-382 (2008).

352   45. Billups, K., York, K. & Bradtmiller, L.I. Water Column Stratification in the Antarctic

353   Zone of the Southern Ocean During the Mid-Pleistocene Climate Transition.

354   *Paleoceanography and Paleoclimatology* **33**, doi:10.1029/2018PA003327 (2018).

355   46. Cheng, W., Chiang, J.C.H. & Zhang, D. Atlantic Meridional Overturning Circulation

356   (AMOC) in CMIP5 Models: RCP and Historical Simulations. *J. Clim.* **26**, 7187-

357   7197, doi:10.1175/jcli-d-12-00496.1 (2013).

358   47. IPCC. *Climate Change 2013: The Physical Science Basis. Contribution of Working*

359   *Group I to the Fifth Assessment Report of the Intergovernmental Panel on*

360 *Climate Change* [Stocker, T.F. *et al*. (eds.)]. Cambridge University Press,

361 Cambridge, United Kingdom and New York, NY, USA. 1535 pp.

362 doi:10.1017/CBO9781107415324 (2013).

363 48. Bernadello, R., Marinov, I., Palter, J.B., Sarmiento, J.L., Galbraith, E.D. & Slater,

364 R.D. Response of the Ocean Natural Carbon Storage to Projected Twenty-First-

365 Century Climate Change. *J. Clim.* **27**, 2033-2053, doi:10.1175/jcli-d-13-00343.1

366 (2014).

367 49. Pérez, F.F., Mercier, H., Vázquez-Rodríguez, M., Lherminier, P., Velo, A., Pardo,

368 P.C., Rosón, G. & Ríos, A.F. Atlantic Ocean CO_2 uptake reduced by weakening

369 of the meridional overturning circulation. *Nature Geoscience* **6**, 146-152,

370 doi:10.1038/ngeo1680 (2013).

371 50. Schmieder, F., von Dobeneck, T. & Bliel, U. The Mid-Pleistocene climate transition

372 as documented in the deep South Atlantic Ocean: Initiation, interim state and

373 terminal event. *Earth Planet. Sci. Lett.* **179**, 539-549 (2000).

378 **Author Contributions.** JF, LP, BH, MR, and SG designed the study; JF, DK, SJ and DB

379 designed the sampling strategy; JF, LH and HF performed trace element analyses; MJ,

380 MY and JK performed Nd sample processing and isotopic analyses; all authors

381 contributed to interpretation of results and manuscript preparation.

382   **Financial and non-financial competing interests.** The authors declare no financial and

383   non-financial competing interests.

384   **Materials & Correspondence**. Correspondence and materials requests should be

385   directed to Jesse R. Farmer (jesse.farmer@princeton.edu).

386   **Figure Captions.**

387   **Figure 1. Location of sediment cores and modern Atlantic Ocean hydrography**. a) Site

388   1267[20] (cyan star) is located in the South Atlantic, along with cores comprising the SUSAS

389   stack[50] (gray circles), and Sites 1088 and 1090[12,14,31]. Site 607[13,25] (orange diamond) is located in

390   the North Atlantic. Colours denote surface ocean potential density from World Ocean Atlas 2013

391   data (www.nodc.noaa.gov/OC5/woa13/); white X's denote regions of modern-day deep-water

392   formation. b) Meridional cross-section showing modern-day phosphate (colour) and salinity

393   (contours indicate isolines) (composite of CLIVAR A20 and A13.5, www.clivar.org). Phosphate-

394   poor NADW fills the Angola Basin to >4 km depth, while phosphate-rich AABW inflow is

395   limited by Walvis Ridge. Phosphate-rich Antarctic Intermediate Water (AAIW) extends

396   northward above 2 km depth. Plots created in Ocean Data View (http://odv.awi.de).

397   **Figure 2. Site 1267 and 607 circulation and trace element records across the MPT**. a) Site

398   1267 $\delta^{18}O_b$[21] (black) and $\delta^{13}C_b$[21,22] (brown); red and blue numbers denote interglacial and glacial

399   stages, respectively. b) Site 1267 ε_{Nd}; opposite axis gives corresponding percentage North

400   Atlantic sourced water (NAW, calculation in Methods). c) B/Ca from 607[13,25] (gray circles) and

401   1267 (filled squares); opposite axis gives $\Delta[CO_3^{2-}]$ (Methods). d) Cd/Ca from 607[13] (gray circles)

402   and 1267 (outlined squares); opposite axis gives $[PO_4^{3-}]$ (Methods). Error bars are replicate $1s$,

403   and are greater than long-term internal precision (Methods). Red, blue and gray squares indicate

404   Site 1267 interglacial, glacial and transitional samples, respectively. Horizontal lines in c) and d)

405   indicate modern $\Delta[CO_3^{2-}]$ and $[PO_4^{3-}]$ at 1267 (blue) and 607 (orange). Vertical gray shading

406   highlights MIS 25 through 22.

407   **Figure 3. Changes in ocean CO_2 feedbacks and climate across the MPT**. ΔDIC reconstructed

408   from $\Delta[CO_3^{2-}]$ (a) and $\Delta[PO_4^{3-}]$ (b) at Sites 1267 (filled squares) and 607 (open squares). c) South

409   Atlantic MOC from ε_{Nd} at Sites 1267 (squares) and 1088[12] (circles). Red/blue symbols in a-c

410   indicate interglacials/glacials, respectively. d) pCO_2 from EPICA Dome C[44] (black line), Allan

411   Hills[16] (black bar at 1,000 ka), planktic foraminiferal boron isotopes (red/blue/gray circles are

412   interglacials/glacials/transitional from ref. 15; cyan curve, ref. 11), and modeled[33]. Yellow

413   shading indicates average pCO_2 for 0-420, 420-900, and 950-2,000 ka. e) Terrigenous mass

414   accumulation rate from Site 745 indicating East Antarctic Ice Sheet activity[45]. f) Iron mass

415   accumulation rate in the Subantarctic Atlantic (Site 1090)[31]. g) Eustatic sea level from South

416   Pacific $\delta^{18}O_{sw}$[10] (cyan line) and Mediterranean planktic foraminifer $\delta^{18}O$[17] (yellow points).

417   **Figure 4. Schematics of proposed coupling between cryosphere, Atlantic MOC, and carbon**

418   **cycle responses across the MPT.** Glacial Atlantic MOC cross-sections before and after 950 ka

419   are in a) and c), respectively. b) and d) show Antarctic processes within dashed regions of a) and

420   c). Curved arrows trace AABW and NADW pathways; arrow colour indicates $[PO_4^{3-}]$ (Fig. 1) and

421   thickness indicates deep-water contribution (thicker is greater contribution). RFZ= Romanche

422   Fracture Zone. Red arrows indicate ocean CO_2 release; orange dots indicate dust deposition.

423   Black curved lines in b) and d) indicate brine rejection. EAIS= East Antarctic Ice Sheet. Before

424   950 ka, a smaller EAIS limits Antarctic sea-ice coverage, shortening the path for Antarctic

425   surface waters before subduction, giving a larger fraction of unutilised nutrients in AABW and

426   greater CO_2 release (b). NADW dominates Atlantic MOC (a). After 950 ka, EAIS expands to

427   marine-based margins and sea-ice expands. Antarctic surface waters upwell farther north,

428   travelling further before subduction, decreasing $[PO_4^{3-}]$ in AABW and lowering CO_2 outgassing

429   (d). AABW dominates deep Atlantic circulation, effectively trapping CO_2 (cross-hatching, c).

430

Methods

ODP Site 1267 and sample selection. ODP Site 1267 (28°5.89' S, 1°42.66'E, 4.36 km water depth) was cored near the northwestern margin of Walvis Ridge in the Angola Basin[20]. Site 1267 chronology was established by aligning *Cibicidoides wuellerstorfi* $\delta^{18}O$[21] to the LR04 global $\delta^{18}O_b$ stack[51]. For this study, *C. wuellerstorfi* specimens >250 µm were picked from samples reflecting glacial-interglacial extremes (indicated by $\delta^{18}O_b$) spanning MIS 46 to MIS 12, and every 25 cm (every ~3 kyr) between MIS 30 and MIS 22 (Supplementary Fig. 4). Our records do not extend beyond MIS 12 due to limited *C. wuellerstorfi* in younger sediments. Glacial and interglacial extremes in B/Ca and Cd/Ca records from Site 607[13,25] were also selected based on $\delta^{18}O_b$ (Supplementary Fig. 4).

Trace element analyses. For Site 1267, six to twelve *C. wuellerstorfi* specimens were crushed between two methanol-cleaned glass slides and transferred to HCl-cleaned 0.5 mL polypropylene vials. When necessary, adjacent samples were combined to provide 200 to 300 µg of calcite. Crushed samples were cleaned via clay removal in methanol and boron-free MilliQ water, removal of Fe-Mn oxides and authigenic Mn carbonates by reduction with an ammonium-citric acid-buffered hydrazine ($NH_4(OH)$-$C_6H_8O_7$-N_2H_4) solution, organic oxidation with NaOH-buffered H_2O_2, and a weak acid leach with 0.001 N HNO_3 to remove any adsorbed contaminants, following standard protocols[52-54]. Samples were transferred to HCl-cleaned 2 mL polypropylene vials after the oxidation step. Initial tests showed elevated Mn and Fe concentrations (> 100 µmol/mol) without reductive cleaning, and thus reductive cleaning was performed on all samples. Removal of Fe and Mn phases is critical for reducing Cd blank[53] and does not affect B/Ca ratios[55]. All sample preparation was performed in a boron-free HEPA laminar flow bench at the Lamont-Doherty Earth Observatory (LDEO).

Cleaned samples were dissolved in 0.8 to 1.6 mL of ultrapure 2% HNO_3 immediately prior to analysis, with the volume of acid adjusted by sample mass to obtain ~50 ppm $[Ca^{2+}]$ solutions. Trace element intensities were measured using a Thermo Scientific iCAP Q inductively coupled plasma mass spectrometer at LDEO[56] following methods adapted from ref. 57. Low mass element ^{11}B was measured in standard mode;

461   ^{23}Na, ^{27}Al, ^{43}Ca, ^{55}Mn, ^{56}Fe, and ^{111}Cd were measured in kinetic energy discrimination

462   mode using a He collision cell to minimise polyatomic interferences. To minimise matrix

463   effects, element intensities were corrected with an internal multi-element quality control

464   standard measured every ten samples. Concentrations and element ratios (relative to Ca)

465   were calculated from element intensities measured on a multi-element stock solution

466   prepared gravimetrically from trace element-grade stock solutions. This solution was

467   diluted to $[Ca^{2+}]$ of 5 to 125 ppm and each dilution was then measured, creating

468   calibrations of element intensity to concentration. External precision was evaluated using

469   nine full procedural replicates from Site 1267, with 1s pooled replicate precision of ±6.6

470   μmol/mol for B/Ca and ±0.009 μmol/mol for Cd/Ca. Long-term internal precision (1s) of

471   an in-house quality control standard was ±2.9 μmol/mol for B/Ca and ±0.006 μmol/mol

472   for Cd/Ca.

473   Site 607 B/Ca and Cd/Ca ratios were previously measured via similar

474   protocols[13,25]. Pooled replicate precision (1s) for Site 607 B/Ca and Cd/Ca was ±5.9 and

475   ±0.007 μmol/mol, respectively[13]. No attempt was made to correct for laboratory B/Ca or

476   Cd/Ca offsets. If laboratory offsets existed, they would not change the results of our study

477   because each core was measured in separate laboratories and we independently calculate

478   ΔDIC from B/Ca and Cd/Ca variations within each core (see below).

479   **Neodymium isotope analyses.** Nd isotopes (^{143}Nd/^{144}Nd) were measured on Fe-Mn

480   encrusted planktic foraminifera[12,58]. Between 20 and 30 mg of planktic foraminifera from

481   the >300 μm size fraction were crushed, ultrasonicated and resuspended in MilliQ water

482   and methanol to remove detrital contaminants. Each sample was treated individually to

483   ensure that sufficient rinsing steps were applied. Cleaned fragments were dissolved in

484   dilute acetic acid, and the resulting solution centrifuged. The supernatant was transferred

485   to clean PFA beakers and Nd was separated using Eichrom Tru-Spec and Ln-Spec resins.

486   Nd isotopes were determined by multi-collector inductively coupled mass spectrometry

487   on a ThermoScientific Neptune-Plus at LDEO. Instrumental drift was corrected by

488   sample-standard bracketing (SSB) using JNdi-1 as the primary standard[59], with matching

489   standard and sample Nd concentrations. Nd isotopes are expressed as ε_{Nd} values, which

490   give deviations in parts per 10^4 from the average ^{143}Nd/^{144}Nd value of chondritic

491 meteorites (0.512638)[60]. External analytical reproducibility $(\pm 2s)$ was 0.28 and 0.43 εNd

492 units $(\pm 0.000014$ and 0.000021 absolute) for the two analytical sessions where Site 1267

493 samples were measured.

494 **Converting B/Ca, Cd/Ca to DIC$_{resp}$.** Global coretop calibration shows that *C.*

495 *wuellerstorfi* B/Ca records $\Delta[CO_3^{2-}]$[23,61-63], where $\Delta[CO_3^{2-}] = [CO_3^{2-}]_{in\ situ} - [CO_3^{2-}]_{saturation}$.

496 Site 607 and 1267 B/Ca was converted to $\Delta[CO_3^{2-}]$ using B/Ca (μmol/mol) = 1.14±0.04*

497 $\Delta[CO_3^{2-}]$ (μmol/kg) + 176.6±1.0 (ref. 63).

498   Both $[CO_3^{2-}]_{in\ situ}$ and $[CO_3^{2-}]_{saturation}$ are relatively insensitive to changes in

499 temperature, salinity, and pressure. For instance, projected changes in deep ocean

500 temperature, salinity and pressure on glacial-interglacial timescales negligibly influence

501 $\Delta[CO_3^{2-}]$ compared to instrumental B/Ca precision[64]. Therefore, downcore changes in

502 $\Delta[CO_3^{2-}]$ primarily reflect changes in deep ocean $[CO_3^{2-}]_{in\ situ}$ driven by changes in the

503 difference between total alkalinity (TA) and dissolved inorganic carbon (DIC)

504 (Supplementary Fig. 2; ref. 27). If the quantity TA-DIC increases, the greater excess of

505 TA relative to DIC implies a shift in DIC speciation toward CO_3^{2-} and thus increased

506 $[CO_3^{2-}]$. Conversely, a decrease in the quantity TA-DIC implies DIC speciation shifts

507 toward CO_2, and thus $[CO_3^{2-}]$ decreases.

508   Changes in $\Delta[CO_3^{2-}]$ at Sites 1267 and 607 are a function of TA and DIC

509 (Supplementary Fig. 2):

510 $$\left(\Delta[CO_3^{2-}]_{measured} - \Delta[CO_3^{2-}]_{reference}\right) = 0.54 * (\Delta TA - \Delta DIC) \qquad (1)$$

511 where $\Delta[CO_3^{2-}]_{measured}$—$\Delta[CO_3^{2-}]_{reference}$ gives the $\Delta[CO_3^{2-}]$ difference from a reference

512 $\Delta[CO_3^{2-}]$ value (here, the average pre-950 ka interglacial $\Delta[CO_3^{2-}]$ of +14.8 μmol/kg at

513 Site 1267 and +39.7 μmol/kg at Site 607), and ΔTA and ΔDIC are the differences in TA

514 and DIC between each sample relative to average pre-950 ka interglacial TA and DIC.

515 Note that while we use $\Delta[CO_3^{2-}]$ instead of $[CO_3^{2-}]_{in\ situ}$ (as used by ref. 27 and 52),

516 Equation 1 is identical using either parameter because $[CO_3^{2-}]_{saturation}$ is assumed constant

517 due to the small influence of temperature, salinity, and pressure variations on $[CO_3^{2-}$

518 $]_{saturation}$ (see above). The slope of Equation 1 (k=0.54) is less than one due to a larger

519   contribution from non-carbonate species (particularly borate anion) to TA as the quantity

520   TA-DIC increases. We calculated k by varying TA and DIC at the present-day bottom-

521   water temperature (2.4°C), salinity (34.89) and pressure (4429 dbar) of Site 1267 in

522   CO2SYS (ref. 65). Following this for Site 607 also returns k of 0.54. In contrast, Yu et

523    $al.$[27] used k=0.59 from regression of oceanographic data below 2.5 km depth in the

524   Atlantic Ocean, but this approach includes influences from pressure, temperature, and

525   salinity variations within the dataset used for their regression. Our slope is more

526   appropriate because the expected temperature, salinity and pressure variations at Sites

527   1267 and 607 across the late Pleistocene are smaller than the present-day ranges of these

528   parameters in the Atlantic Ocean below 2.5 km depth.

529   Two processes primarily control deep ocean TA and DIC: organic matter

530   respiration and calcium carbonate ($CaCO_3$) dissolution (Supplementary Fig. 2). Explicitly

531   accounting for the effects of respiration and dissolution in Eq. 1 and substituting pre-950

532   ka interglacial $\Delta[CO_3^{2-}]$ for $\Delta[CO_3^{2-}]_{reference}$ gives:

533    $$\left(\Delta[CO_3^{2-}]_{measured} - 14.8\right) = 0.54 * \left((\Delta TA - \Delta DIC)_{resp} + (\Delta TA - \Delta DIC)_{diss}\right) \qquad (2)$$

534   for Site 1267. (For Site 607, 39.7 μmol/kg is subtracted from $\Delta[CO_3^{2-}]_{measured}$ to

535   normalize to average pre-950 ka interglacial $\Delta[CO_3^{2-}]$). Here $resp$ and $diss$ denote

536   changes from organic matter respiration and dissolution, respectively. Respiring 1 μmol

537   of organic matter in 1 kg seawater increases DIC by 1 μmol/kg and decreases TA by 0.14

538   μmol/kg (ref. 26). This decreases the quantity TA-DIC by 1.14 μmol/kg and thus

539   decreases $[CO_3^{2-}]_{in\ situ}$ by 0.62 μmol/kg. Dissolution of 1 μmol of $CaCO_3$ in 1 kg seawater

540   increases DIC by 1 μmol/kg and increases TA by 2 μmol/kg, which increases TA-DIC by

541   1 μmol/kg and thus raises $[CO_3^{2-}]_{in\ situ}$ by 0.54 μmol/kg. Using these stoichiometric ratios

542   of TA- and DIC-change during respiration and dissolution, Eq. 2 becomes:

543    $$\left(\Delta[CO_3^{2-}]_{measured} - 14.8\right)(\mu mol / kg) = 0.54 * \left(0.5\Delta TA_{diss} - 1.14\Delta DIC_{resp}\right) \qquad (3)$$

544   for Site 1267. As in Eq. 1, ΔTA_{diss} and ΔTA_{resp} values are calculated relative to pre-950

545   ka interglacial averages.

546   Equation 3 has three unknowns: $\Delta[CO_3^{2-}]$, ΔTA_{diss}, and ΔDIC_{resp}. B/Ca constrains

547    $\Delta[CO_3^{2-}]$, but one more constraint is required to solve Eq. 3. One approach is to assume

548   constant deep ocean alkalinity[27] (ΔTA_{diss}=0), which allows Eq. 3 to be solved for

549   ΔDIC_{resp}. Previous applications of B/Ca to reconstruct DIC assumed constant TA over

550   short study intervals[27,66] (<50 kyr). In contrast, our 1-Myr record covers a climate

551   transition associated with notable changes in deep-sea carbonate sedimentation[25,49,67]

552   (Supplementary Fig. 5). Thus, it may not be practical to assume that ΔTA_{diss}=0 (see

553   below).

554   Lacking established paleo-proxies for TA, here we also calculate ΔDIC_{resp} using

555   *C. wuellerstorfi* Cd/Ca, an independent nutrient proxy that is unlikely affected by ΔTA_{diss}.

556   *Cibicidoides wuellerstorfi* Cd/Ca relates to deep ocean [Cd] through the following

557   relationship:

558    $$[Cd]_{sw}(nmol/kg) = \frac{10*(Cd/Ca)_{C.wuellerstorfi}}{2.9} \qquad (4)$$

559   where 2.9 is the partition coefficient of Cd into calcitic foraminifera below 3 km depth

560   and 10 is the seawater [Ca^{2+}] in mmol/kg[24,68,69]. [Cd]$_{sw}$ relates to [DIC]$_{resp}$ through

561   stoichiometric relationships in seawater and organic matter. In the modern Atlantic Ocean,

562   [Cd]$_{sw}$ is strongly, but nonlinearly, correlated with phosphate concentration ([PO$_4^{3-}$])[70-73].

563   This nonlinearity might reflect Cd uptake by phytoplankton[71] possibly modulated by the

564   local abundance of other trace elements[72]. Recent high-quality [Cd]$_{sw}$ measurements

565   taken during the GEOTRACES program in the Atlantic Ocean[72-75] exhibit a strong

566   nonlinear correlation to [PO$_4^{3-}$], which is linearized by using the square root of [Cd]$_{sw}$

567   (Supplementary Fig. 2c):

568    $$[PO_4^{3-}](\mu mol/kg) = \frac{\sqrt{[Cd]_{sw}} - 0.062}{0.361} \qquad (5)$$

569   *Cibicidoides wuellerstorfi* Cd/Ca is used to calculate $\Delta[Cd]_{sw}$ using Equation 4,

570   and then ΔDIC_{resp} associated with $\Delta[Cd]_{sw}$ is calculated assuming a Redfield C:P ratio of

571   117±14:1 (ref. 26):

572
$$\Delta DIC_{resp}(\mu mol / kg) = (117 \pm 14) * \frac{\sqrt{\Delta [Cd]_{sw}} - 0.062}{0.361}$$
(6)

573 As in Equation 3, ΔDIC_{resp} and $\Delta[Cd]_{sw}$ are calculated as differences relative to pre-950

574 ka interglacial averages.

575   Reconstructed ΔDIC_{resp} from Cd/Ca (Equation 6) largely agrees with ΔDIC_{resp}

576 calculated from B/Ca (Equation 3) assuming ΔTA_{diss}=0 over our study interval at Site

577 1267 (Supplementary Fig. 6). This correspondence argues against major variations in

578 uncertainty sources that affect one—but not both—proxies. Specifically, this

579 correspondence suggests that any changes in ΔTA_{diss} (influencing B/Ca) are smaller than

580 the (relatively large) uncertainty on B/Ca-derived ΔDIC_{resp} (discussed below). Similarly,

581 this argues against secondary influences on Cd/Ca-derived ΔDIC_{resp} estimates

582 (Supplementary Information).

583 **Quantifying deep Atlantic carbon storage.** Following ref. 27, we quantify deep

584 Atlantic carbon storage as follows:

585
$$\Delta C(Gt) = \frac{-12.011 * \Delta DIC_{Atlantic>3km} * m_{Atlantic>3km}}{10^{21}}$$
(7)

586 where $\Delta DIC_{Atlantic>3km}$ is the pooled average DIC increase at Sites 1267 and 607 in

587 µmol/kg (42±15 µmol/kg for glacials and 30±16 µmol/kg for interglacials), $m_{Atlantic>3km}$ is

588 the mass of water in the Atlantic Ocean below 3 km depth ($1.01*10^{20}$ kg), 12.011 is the

589 mass of carbon (g/mol), and factor 10^{21} converts units from µg C to Gt C[76]. This

590 calculation assumes that the magnitude of DIC increase reconstructed from Sites 1267

591 and 607 characterises the entire Atlantic Ocean below 3 km.

592 **Significance Testing.** Statistical comparisons of mean glacial/interglacial ε_{Nd} and

593 reconstructed DIC before and after 950 ka was performed using one-tailed, two-sample t-

594 test with unequal variance (Welch's t-test) in MATLAB (function ttest2). Significance

595 was evaluated with α=0.05. Mean values and p-values for statistical tests are given in

596 Supplementary Table 1.

597 **Influence of alkalinity on pCO$_2$.** Records of deep ocean sedimentary CaCO$_3$ content

598 suggest pronounced changes in CaCO$_3$ sedimentation at the MPT. Expanded AABW

599 resulting from reduced MOC lowered CaCO$_3$ preservation throughout the deep Atlantic

600 at the MPT, as evidenced by carbonate %[25], sediment lightness (L*) and magnetic

601 susceptibility records[50] (Supplementary Fig. 5). However, Site 1267 and 607 $\Delta[CO_3^{2-}]$

602 reconstructions do not show clear evidence for a transient $\Delta[CO_3^{2-}]$ rise across the MOC

603 reduction (Fig. 2), as might be expected to occur within 5-10 kyr from "classic"

604 carbonate compensation[39]. Site 1267 has an average sampling resolution of 9.2 kyr

605 between 1,000 and 875 ka, and it is possible that this record lacks sufficient resolution to

606 reconstruct a rapid carbonate compensation event. Site 607 has an average resolution of

607 ~3 kyr, yet also does not show transient $\Delta[CO_3^{2-}]$ rises[25].

608 One possibility is that any $\Delta[CO_3^{2-}]$ rise from carbonate compensation is masked

609 within these records; i.e., $\Delta[CO_3^{2-}]$ decreases less than expected from DIC increase alone

610 due to the counteracting influence of increased TA from regional carbonate dissolution.

611 In this scenario, ΔDIC derived from B/Ca would systematically underestimate true ΔDIC.

612 To quantify this underestimation, Equation 3 shows that a 1 μmol/kg increase in TA from

613 CaCO$_3$ dissolution increases $\Delta[CO_3^{2-}]$ by 0.27 μmol/kg. Estimates of the TA contribution

614 from CaCO$_3$ dissolution in the modern ocean (termed TA*, ref. 77) show TA* of 0-10

615 μmol/kg for NADW and 20-30 μmol/kg for AABW. Assuming that the MOC shift at Site

616 1267 was associated with a 30 μmol/kg TA increase from enhanced CaCO$_3$ dissolution,

617 $\Delta[CO_3^{2-}]$ would increase by 8.1 μmol/kg. This increase equates to ΔDIC of -13 μmol/kg,

618 giving a revised post-950 ka glacial ΔDIC estimate of 63±16 μmol/kg from $\Delta[CO_3^{2-}]$

619 from Sites 1267 and 607, which is indistinguishable from the $\Delta[PO_4^{3-}]$-derived ΔDIC

620 estimate of 49±24 μmol/kg.

621 Based on Site 607 $\Delta[CO_3^{2-}]$, Sosdian et al.[25] present a new model of carbonate

622 compensation driven by changes in regional carbonate burial, and not local dissolution. In

623 this model, the relationship between deep Atlantic TA and global ocean TA depends on

624 Pacific CaCO$_3$ burial, giving a more complex relationship between deep Atlantic TA and

625 potential CO$_2$ drawdown. Regardless, while the precise magnitude of ΔDIC may be

626 sensitive to TA change from carbonate compensation and compensation mechanisms, the

28

627 conclusion of increased DIC in the deep Atlantic coeval with reduced MOC is not

628 contingent on assuming constant TA.

629 **Mixing between NADW and AABW.** Supplementary Figure 3 shows relationships

630 between Site 1267 $[PO_4^{3-}]$, $[CO_3^{2-}]$, $\delta^{13}C$[22], and relative NADW/AABW contributions

631 from ε_{Nd}. Mixing curves are calculated using modern day endmember values for NADW

632 and AABW defined from hydrographic data for ε_{Nd}, $[PO_4^{3-}]$ and $[CO_3^{2-}]$, and using late

633 Holocene benthic foraminifer $\delta^{13}C$ for $\delta^{13}C_{DIC}$. Foraminifera were chosen to define the

634 $\delta^{13}C_{DIC}$ endmembers considering the impact of anthropogenic carbon on hydrographic

635 $\delta^{13}C_{DIC}$ (the 'Suess effect'), particularly in NADW[78]. Endmember values for ε_{Nd} and

636 [Nd]: NADW = -14.0±0.5 ε units and [Nd] = 23.6 pmol/kg, AABW = -8.0±0.5 ε units

637 and [Nd] = 26.1 pmol/kg (Y. Wu, pers. comm.); $[PO_4^{3-}]$: NADW = 1.1±0.05 μmol/kg,

638 AABW = 2.25±0.01 μmol/kg[74]; $[CO_3^{2-}]$: NADW = 120±10 μmol/kg, AABW = 85±5

639 μmol/kg[74]; $\delta^{13}C$: NADW = 1.36±0.08‰ (0-5 ka from BOFS 11K, ref. 64); AABW =

640 0.27±0.1‰ (coretop from TN057-21; ref. 79). Mixing curves are calculated from simple

641 two-component concentration and isotope mixture equations (example below for ε_{Nd}):

642
$$\varepsilon_{Nd\_mixture} = \frac{f_{NADW}*[Nd]_{NADW}*\varepsilon_{Nd\_NADW} + f_{AABW}*[Nd]_{AABW}*\varepsilon_{Nd\_AABW}}{f_{NADW}*[Nd]_{NADW} + f_{AABW}*[Nd]_{AABW}} \qquad (8)$$

643 **Preformed nutrients in AABW.** In NADW and AABW endmembers, $[PO_4^{3-}]$ is

644 composed of preformed PO_4^{3-} and regenerated PO_4^{3-} components[80,81]:

645
$$[PO_4^{3-}]_{total}(\mu mol/kg) = [PO_4^{3-}]_{preformed} + [PO_4^{3-}]_{regenerated} \qquad (9)$$

646 Following ref. 82, we use $[PO_4^{3-}]_{preformed}$ of 0.8 μmol/kg for NADW and 1.5

647 μmol/kg for AABW. These values agree with $[PO_4^{3-}]_{preformed}$ calculated from

648 GEOTRACES[74] apparent oxygen utilisation (AOU) data ($[PO_4^{3-}]_{preformed}$ of 0.78±0.03 and

649 1.57±0.03 μmol/kg for NADW and AABW, respectively, using AOU of 55±5 and 115±5

650 μmol/kg for NADW and AABW, respectively, and an O_2:PO_4^{3-} ratio of 170 from ref. 26;

651 calculation in ref. 82).

652 Additional curves in Supplementary Figure 3 show mixing between modern

653 NADW and AABW with $[PO_4^{3-}]_{preformed}$ reduced by 25% and 50%, giving AABW $[PO_4^{3-}$

654   ]$_{preformed}$ of 1.13 and 0.9 µmol/kg, respectively. Note that [PO$_4^{3-}$]$_{total}$ is kept constant, any

655   [PO$_4^{3-}$]$_{preformed}$ decrease is added to [PO$_4^{3-}$]$_{regenerated}$[81]. The addition of [PO$_4^{3-}$]$_{regenerated}$ adds

656   regenerated DIC, increasing DIC (117:1 ratio[26]), and thus decreasing [CO$_3^{2-}$]. The effect

657   of DIC addition on [CO$_3^{2-}$] is calculated using Equation 3 (above). The effect on δ^{13}C is

658   calculated by assuming the added DIC possesses a constant δ^{13}C of -25‰ corresponding

659   to organic matter. Two-component mixing curves are then recalculated using the modern-

660   day NADW endmember values and the updated AABW endmember [CO$_3^{2-}$] and δ^{13}C

661   values.

662   Cross-plots of [PO$_4^{3-}$], [CO$_3^{2-}$] and δ^{13}C with ε_{Nd} show that reconstructed [PO$_4^{3-}$]

663   corresponds to mixing between modern NADW and AABW endmembers, while [CO$_3^{2-}$]

664   and benthic δ^{13}C imply mixing with AABW possessing lower [CO$_3^{2-}$] and δ^{13}C$_{DIC}$ than

665   modern (Supplementary Fig. 3). These observations can be reconciled by a higher

666   regenerated to preformed PO$_4^{3-}$ ratio in mid-Pleistocene AABW compared to today. A

667   shift from [PO$_4^{3-}$]$_{preformed}$ to [PO$_4^{3-}$]$_{regenerated}$ would not change total [PO$_4^{3-}$][81], but would

668   decrease AABW [CO$_3^{2-}$] and δ^{13}C through excess regenerated ^{13}C-depleted organic

669   matter and sluggish air-sea gas exchange in the Southern Ocean. Mixing arrays calculated

670   with varying regenerated to preformed PO$_4^{3-}$ ratios suggest that AABW in the Angola

671   Basin may have had up to 50% lower [PO$_4^{3-}$]$_{preformed}$ during the MPT compared to today,

672   particularly in glacials after 950 ka (Supplementary Fig. 3). This level of decreased

673   AABW [PO$_4^{3-}$]$_{preformed}$ is similar to estimates for the Last Glacial Maximum (LGM)[81],

674   when AABW δ^{13}C and Δ[CO$_3^{2-}$] were lower than today[14,63], and is consistent with the

675   proposed coupling between Southern Ocean nutrient utilisation and expanded AABW

676   through Southern Ocean surface buoyancy forcing[38].

677   Because modern AABW has more preformed nutrients than NADW, assuming

678   that modern AABW expanded in the past would have ventilated a greater portion of the

679   deep Atlantic through the Southern Ocean, where the biological pump is less efficient. In

680   this scenario, reduced MOC would both increase deep Atlantic DIC and increase

681   pCO$_2$[29,80]. For the MPT, if expanded AABW possessed 50% lower [PO$_4^{3-}$]$_{preformed}$, the

682   effect of preformed nutrients on pCO$_2$ would be minor. This is because AABW would

683   replace NADW of similar [PO$_4^{3-}$]$_{preformed}$, implying that deep Atlantic [PO$_4^{3-}$]$_{preformed}$

684 stayed relatively constant. This is critical for pCO_2 because it implies that reduced MOC

685 was not associated with a less efficient biological pump, and further implies that reduced

686 MPT pCO_2 required coupling between MOC and CO_2 outgassing in the Southern Ocean

687 (Fig. 4).

688 **Data availability.** The datasets generated during the current study are available as

689 Supplementary Tables 2 through 5 in the Supplementary Data, and will be publicly

690 accessible via the National Centers for Environmental Information (NCEI) following

691 acceptance. A persistent web link to the dataset will be provided at that time.
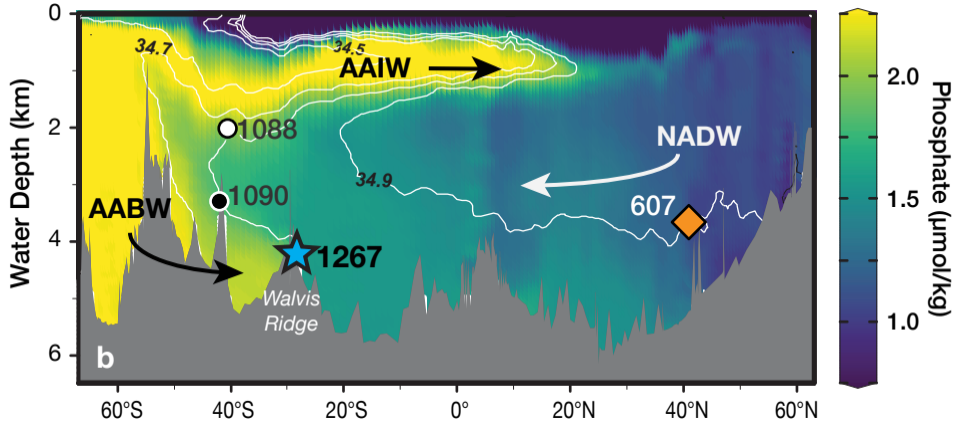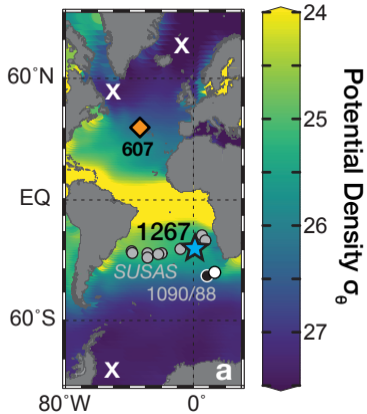
692

693 **Methods References.**

694 51. Lisiecki, L.E., & Raymo, M.E. A Pliocene-Pleistocene stack of 57 globally

695   distributed benthic $\delta^{18}O$ records. *Paleoceanography* **20**, PA1003 (2005).

696 52. Yu, J. *et al.* Responses of the deep ocean carbonate system to carbon reorganization

697   during the Last Glacial-interglacial cycle. *Quat. Sci. Rev.* **76**, 39-52 (2013).

698 53. Rosenthal, Y., Boyle, E.A., & Labeyrie, L. Last glacial maximum paleochemistry and

699   deepwater circulation in the Southern Ocean: Evidence from foraminiferal

700   cadmium. *Paleoceanography* **12**, 787-796 (1997).

701 54. Barker, S., Greaves, M., & Elderfield, H. A study of cleaning procedures used for

702   foraminiferal Mg/Ca paleothermometry. *Geochem. Geophys. Geosyst.* **4**, 8407

703   (2003).

704 55. Yu, J., Elderfield, H., Greaves, M., & Day, J. Preferential dissolution of benthic

705   foraminiferal calcite during laboratory reductive cleaning. *Geochem. Geophys.*

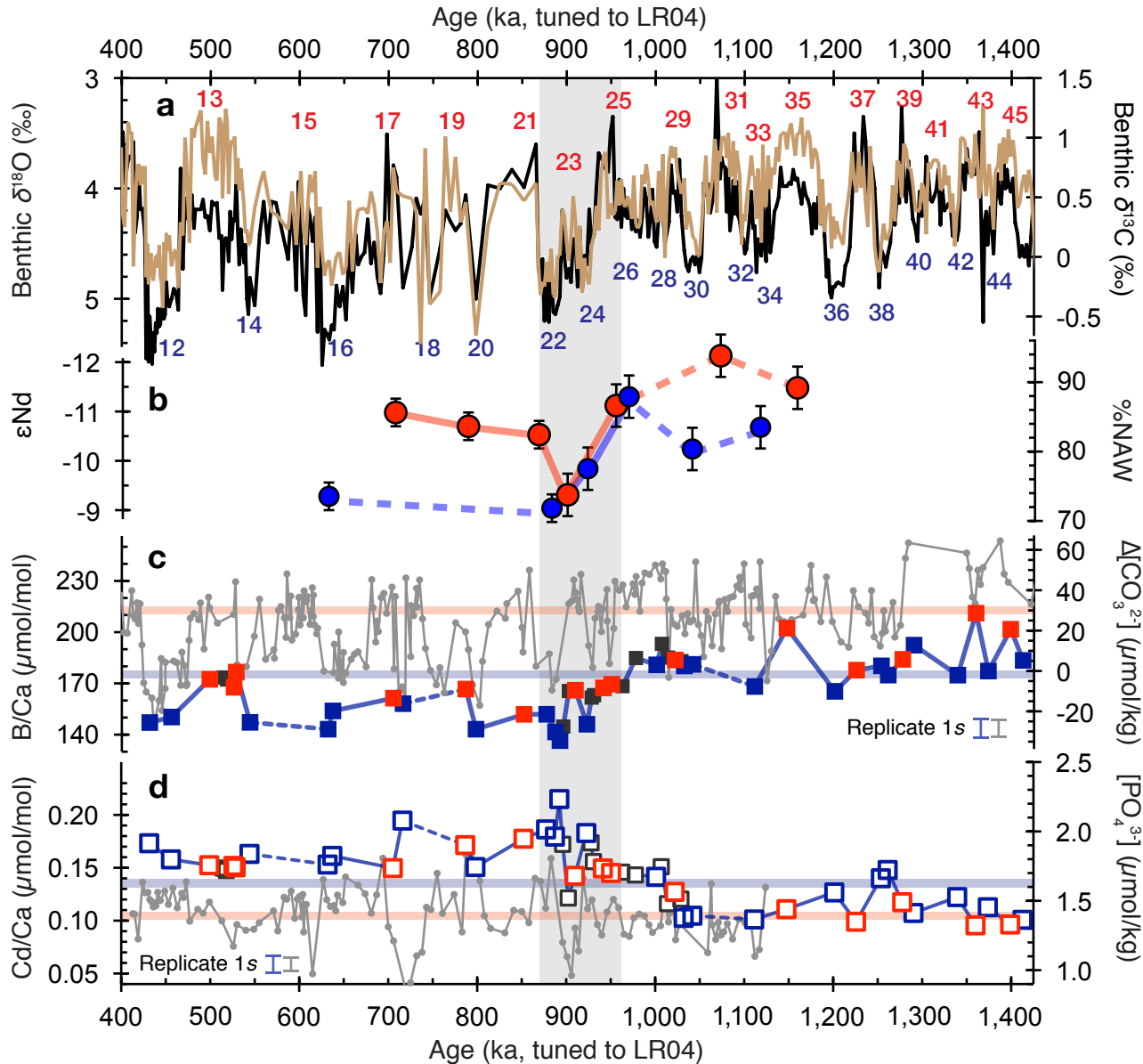706   *Geosyst.* **8**, Q06016 (2007).

707   56. Ford, H.L., Sosdian, S.M., Rosenthal, Y., & Raymo, M.E. Gradual and abrupt

708   changes during the Mid-Pleistocene Transition. *Quat. Sci. Rev.* **148**, 222-233

709   (2016).

710   57. Yu, J., Day, J., Greaves, M., & Elderfield, H. Determination of multiple

711   element/calcium ratios in foraminiferal calcite by quadrupole ICP-MS. *Geochem.*

712   *Geophys. Geosyst.* **6**, Q08P01 (2005).

713   58. Roberts, N.L., Piotrowski, A.M., McManus, J.F., & Keigwin, L.D. Synchronous

714   deglacial overturning and water mass source changes. *Science* **327**, 75-78 (2010).

715   59. Tanaka, T. *et al.* JNdi-1: a neodymium isotopic reference in consistency with LaJolla

716   neodymium. *Chem. Geol.* **168**, 279-281 (2000).

717   60. Jacobsen, S.B. & Wasserburg, G.J. Sm-Nd isotopic evolution of chondrites. *Earth*

718   *Planet. Sci. Lett.* **50**, 139-155 (1980).

719   61. Rae, J.W.B., Foster, G.L., Schmidt, D.N. & Elliott, T. Boron isotopes and B/Ca in

720   benthic foraminifera: Proxies for the deep ocean carbonate system. *Earth Planet.*

721   *Sci. Lett.* **302**, 403-413 (2011).

722   62. Raitzsch, M., Hathorne, E.C., Kuhnert, H., Groeneveld, J. & Bickert, T. Modern and

723   late Pleistocene B/Ca ratios of the benthic foraminifer *Planulina wuellerstorfi*

724   determined with laser ablation ICP-MS. *Geology* **39**, 1039-1042 (2011).

725   63. Yu, J. *et al.* Responses of the deep ocean carbonate system to carbon reorganization

726   during the Last Glacial-interglacial cycle. *Quat. Sci. Rev.* **76**, 39-52 (2013).
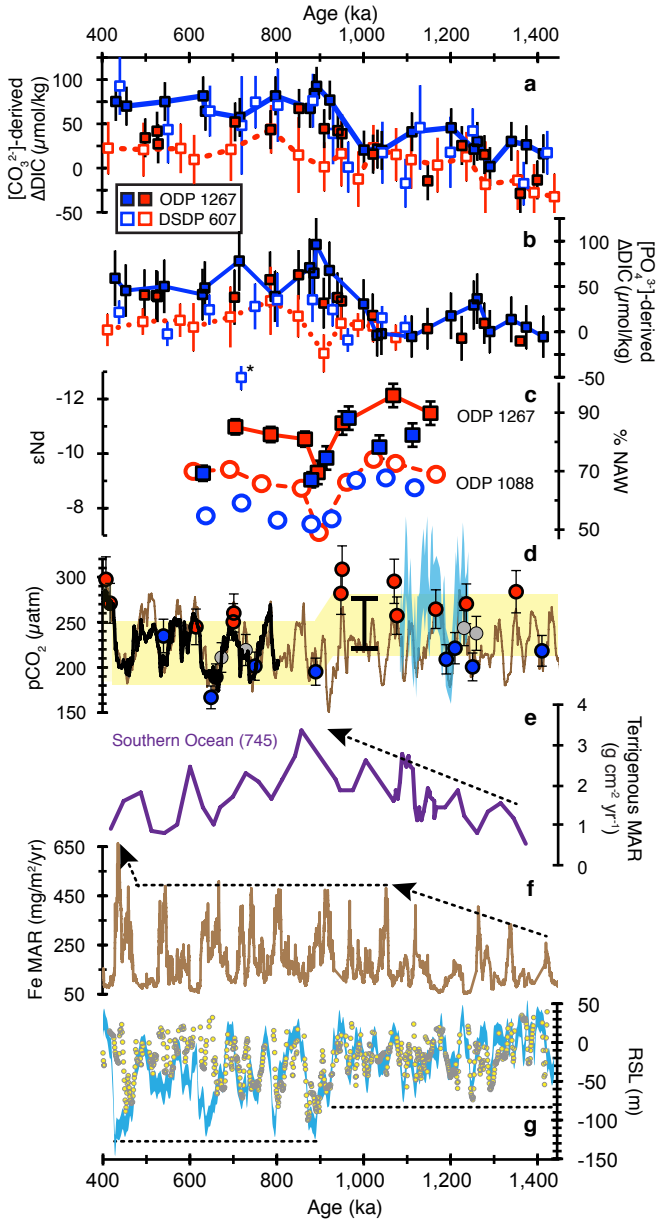
727   64. Yu, J., Elderfield, H. & and Piotrowski, A. Seawater carbonate ion-δ^{13}C systematics

728   and application to glacial-interglacial North Atlantic Ocean circulation. *Earth*

729   *Planet. Sci. Lett.* **271**, 209-220 (2008).

730   65. van Heuven, S., Pierrot, D., Rae, J.W.B., Lewis, E., & Wallace, D.W.R. MATLAB

731   Program Developed for CO2 System Calculations. ORNL/CDIAC-105b. Carbon

732   Dioxide Information Analysis Center, Oak Ridge National Laboratory, U.S.

733   Department of Energy, Oak Ridge, Tennessee (2011).

734   66. Yu, J. *et al*. Loss of Carbon from the Deep Sea since the Last Glacial Maximum.

735   *Science* **330**, 1084-1087 (2010).

736   67. Sexton, P.F. & Barker, S. Onset of 'Pacific-style' deep-sea sedimentary carbonate

737   cycles at the mid-Pleistocene transition. *Earth Planet. Sci. Lett.* **321-322**, 81-94

738   (2012).

739   68. Boyle, E.A. Cadmium: Chemical tracer of deepwater paleoceanography.

740   *Paleoceanography* **3**, 471-489 (1988).

741   69. Marchitto, T.M. & Broecker, W.S. Deep water mass geometry in the glacial Atlantic

742   Ocean: A review of constraints from the paleonutrient proxy Cd/Ca. *Geochem.*

743   *Geophys. Geosyst.* **7**, Q12003 (2006).

744   70. de Baar, H.J.W., Saager, P.M., Nolting, R.F., & van der Meer, J. Cadmium versus

745   phosphate in the world ocean. *Mar. Chem.* **46**, 261-281 (1994).

746   71. Elderfield, H., & Rickaby, R.E.M. Oceanic Cd/P ratio and nutrient utilisation in the

747   glacial Southern Ocean. *Nature* **405**, 305-310 (2000).

748   72. Baars, O., Abouchami, W., Galer, S.J.G., Boye, M., & Croot, P.L. Dissolved

749   cadmium in the Southern Ocean: Distribution, speciation, and relation to

750   phosphate. *Limnol. Oceanogr.* **59**, 385-399 (2014).

751   73. Quay, P., & Wu, J. Impact of end-member mixing on depth distributions of δ^{13}C,

752   cadmium and nutrients in the N. Atlantic Ocean. *Deep-Sea Res. II* **116**, 107-116

753   (2015).

754   74. Mawji, E. *et al.*, The GEOTRACES Intermediate Data Product 2014. *Mar. Chem.*

755   **177**, 1-8 (2015).

756   75. Roshan, S., & Wu, J. Cadmium regeneration within the North Atlantic. *Global*

757   *Biogeochem. Cycles* **29**, 2082-2094 (2015).

758   76. Clark, W.C. (ed.) *Carbon Dioxide Review: 1982*, p. 467, Oxford University Press,

759   New York (1982).

760   77. Feely, R.A., Sabine, C.L., Lee, K., Millero, F.J., Lamb, M.F., Greeley, D., Bullister,

761   J.L., Key, R.M., Peng, T.-H., Kozyr, A., Ono, T. & Wong, C.S. In situ calcium

762   carbonate dissolution in the Pacific Ocean. *Global Biogeochem. Cycles* **16**, 1144

763   (2002).

764   78. Olsen, A. & Ninnemann, U. Large δ^{13}C Gradients in the Preindustrial North Atlantic

765   Revealed. *Science* **330**, 658-659, doi:10.1126/science.1193769 (2010).

766   79. Ninnemann, U.S. & Charles, C.D. Changes in the mode of Southern Ocean

767   circulation over the last glacial cycle revealed by foraminiferal stable isotopic

768   variability. *Earth Planet. Sci. Lett.* **201**, 383-396 (2002).
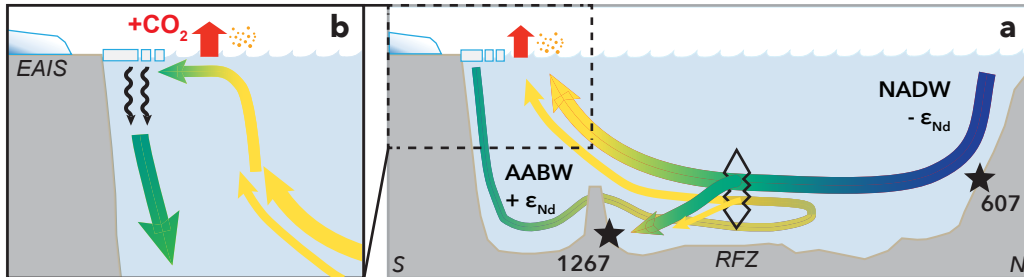
769   80. Marinov, I., Gnanadesikan, A., Sarmiento, J.L., Toggweiler, J.R., Follows, M. &

770   Mignone, B.K. Impact of oceanic circulation on biological carbon storage in the

771   ocean and atmospheric pCO$_2$. *Global Biogeochem. Cycles* **22**, GB3007 (2008).

772   81. Jaccard, S.L., Galbraith, E.D., Sigman, D.M., Haug, G.H., Francois, R., Pedersen,

773   T.F., Dulski, P., & Thierstein, H.R. Subarctic Pacific evidence for a glacial

774   deepening of the oceanic respired carbon pool. *Earth Planet. Sci. Lett.* **277**, 156-

775   165 (2009).

776   82. Broecker, W.S., Takahashi, T., and Takahashi, T. Sources and Flow Patterns of Deep-

777   Ocean Waters as Deduced from Potential Temperature, Salinity, and Initial

778   Phosphate Concentration. *J. Geophys. Res.* **90**, 6925-6939 (1985).

Pre-MPT Glacials (1,400 to 1,000 ka)

a

NADW
$-\varepsilon_{Nd}$

AABW
$+\varepsilon_{Nd}$

607

1267

RFZ

S

N

b

$+CO_2$

EAIS

Post-MPT Glacials (after 950 ka)

c

$[PO_4^{3-}]$ low high

$+ CO_2$ storage

607

1267

RFZ

S

N

d

$- CO_2$